JOTCS A
Journal of the Turkish Chemical Society
Section: A
Chemistry
TURKISH CHEMICAL SOCIETY

Structural and Dielectric Properties of Eu^{3+}, B^{3+} co-doped $CoNb_2O_6$ Ceramic

Mustafa İlhan[1*], Mete Kaan Ekmekçi[2], Kadir Esmer[3]

[1]Department of Environmental Engineering, Faculty of Engineering, Marmara University, Maltepe, 34854, Istanbul, Turkey.
[2]Marmara University, Department of Chemistry, Faculty of Science, Marmara University, Kadıköy, 34722, Istanbul, Turkey.
[3]Department of Physics, Faculty of Science, Marmara University, Kadıköy, 34722, Istanbul, Turkey.

Abstract: The boron co-doped $CoNb_2O_6$:$x$$Eu^{3+}$, $y$$B^{3+}$ (x=1, 3, 6, 9, 12 mol%, y=10 mol%) ceramics were obtained by the molten salt method, which has advantageous properties such as short reaction time, low sintering temperature, improved homogeneity, and crystallinity. The ceramic samples were examined by structural and dielectric analyses. In X-ray diffractions, the orthorhombic columbite type $CoNb_2O_6$ structure was obtained, and also a minor $EuNbO_4$ phase was detected with increasing Eu^{3+} doping concentrations. Additionally, increasing Eu^{3+} concentration led to a slight increase in crystallite size, and two theta peak shifts occurred towards higher angles associated with shrinkage in the lattice or reduction in the lattice constant. In SEM examinations, a slight increase was observed in grain sizes from 1 to 9 mol% Eu^{3+} in the range of 1-30 μm, while some decrease occurred in grain sizes at 12 mol%, and there was an evident increase in plate-shaped and elongated grains. The dielectric constant (ε') of the ceramic samples increased with increasing Eu^{3+} concentration and reached approximately 35 and 0.24 at 20 Hz for 9 mol% Eu^{3+}, respectively. The increase in dielectric loss with increasing Eu^{3+} was associated with an increase in ionic conductivity, in which Eu^{3+} substitution does not suppress oxygen vacancies or make them more ordered.

Keywords: $CoNb_2O_6$, XRD, SEM, Eu^{3+} doping, dielectric properties.

Submitted: November 29, 2023. **Accepted:** February 24, 2024.

Cite this: İlhan M, Ekmekçi MK, Esmer K. Structural and Dielectric Properties of Eu^{3+}, B^{3+} co-doped $CoNb_2O_6$ Ceramic. JOTCSA. 2024;11(2):765-74.

DOI: https://doi.org/10.18596/jotcsa.1397311

***Corresponding author's E-mail:** mustafa.ilhan@marmara.edu.tr

1. INTRODUCTION

Materials exhibiting high dielectric constant are widely used in electronic industries such as capacitors, memory devices, and filters. In practical applications, materials with a high dielectric constant are desired to exhibit low dielectric loss and relatively weak frequency and temperature dependence (1-3). Luminescent dielectrics can be obtained from host materials doped with RE ions. Among the rare earth (RE) ions, the trivalent europium ion is considered an excellent red activator for the luminescence centers of red phosphors due to its $^5D_0$ -^7F_J (J=0, 1, 2, 3, 4) transitions (4-6) and is also widely used in dielectric-related research (7-10). There are some studies on the secondary phase effect on the dielectric properties of rare earth ion-doped host materials. Wang et al (11) investigated the microstructure, and dielectric properties of $(Nd_{0.5}Nb_{0.5})_xTi_{1-x}O_2$ ceramics, and revealed that the secondary phase is beneficial to increase the grain boundary resistance and the material keeps low dielectric loss and improved the temperature stability. In another study, Zhao and Wu (12) examined the dielectric behavior of the $(Dy_{0.5}Nb_{0.5})_xTi_{1-x}O_2$ structure, where the secondary phases are induced by Dy enrichment, and largely facilitate the decreased dielectric loss.

The columbite-type structure with orthorhombic symmetry can be expressed as MNb_2O_6 (M= Co, Mg, Sr, Mn, Ni, Cd, etc). The MNb_2O_6 structure has a significant advantage in that it can host guest ions with ionic sizes comparable to the Nb and divalent M^{2+} ions found in the structure. As MNb_2O_6 structure, cobalt niobate ($CoNb_2O_6$) has been studied due to its magnetic (13-16), neutron scattering (17), luminescence (18-21), dielectric (22,23) gas sensing (24,25) and magnetic-thermodynamic (26,27) properties. Singh et al (22) reported the dielectric and ferroelectric properties of Ti^{4+} doped $CoNb_2O_6$

where Ti^{4+} substitution in $CoNb_2O_6$ lattice enhances the dielectric constant of the material. The dielectric constant (ε') for undoped $CoNb_2O_6$ is found to be 500, whereas $CoNb_{1.95}Ti_{0.05}O_6$ is 700 and $CoNb_{1.9}Ti_{0.1}O_6$ is 14000 at 100 Hz frequency at 200 °C. Zhang et al (23) also studied the sintering behavior and microwave dielectric properties of B_2O_3 doped $CoNb_2O_6$, where the 1.5 wt% B_2O_3 doped $CoNb_2O_6$ sintered at 1000 °C exhibited microwave dielectric properties with an ε' of 22.4, a high Qxf of 43.979 GHz, and a τ_f of -46.2 ppm/°C. In addition, there are studies on the effect of boron on grain morphology and its improvement in dielectric properties in which the doping of boron has the effect of increasing the bulk properties to some extent and can reduce the grain boundaries in the structure (28-30). Moreover, there are also studies on the morphology of lanthanide ion-doped structures with boron addition and the luminescence-enhancing properties of boron (31-33).

In this paper, the structural and dielectric properties of $CoNb_2O_6$:$x$$Eu^{3+}$,$y$$B^{3+}$ (x=1, 3, 6, 9, 12 mol%, y=10 mol%) ceramics fabricated at 900 °C were investigated by doping boron to $CoNb_2O_6$:$x$$Eu^{3+}$ (x=1, 3, 6, 9, 12 mol%) powders produced by the molten salt method at 800 °C. The structural and dielectric analyses were performed by XRD, SEM-EDS, and impedance analyzer.

2. EXPERIMENTAL

The $CoNb_2O_6$:$x$$Eu^{3+}$ (x=0.01, 0.03, 0.06, 0.09, and 0.12 or x=1, 3, 6, 9, 12 mol%) powders were fabricated by the molten salt route. In the synthesis, cobalt nitrate hexahydrate ($Co(NO_3)_2.6H_2O$) (Sigma-Aldrich, 98.5%), niobium oxide (Nb_2O_5) (Alpha Aesar, 99.9%), and europium oxide (Eu_2O_3) (Alpha Aesar, 99.9%) were used. For the synthesis, Li_2SO_4/Na_2SO_4 (salt/salt), and $Li_2SO_4+Na_2SO_4/CoO+Nb_2O_5+Eu_2O_3$ (salt/oxide) molar ratio were taken as 0.635/0.365 and 2/1 weight ratio, respectively. The oxide mixtures and salt mixtures were prepared according to their stoichiometric ratios and mixed well in an agate mortar to provide homogeneity. The resulting mixtures were subsequently placed in an alumina crucible and sintered for 4 h at 800 °C in an air atmosphere using an electric furnace. After the sintering, the ceramic powders were washed down several times with bi-distilled water to get rid of the ionic salts and filtered using a vacuum pump several times. The remnants of Cl^- ions in the solution were controlled by qualitative analysis. To investigate the structural and dielectric properties, the 10 mol% boron in the form of H_3BO_3 was added to the synthesized powders, pelletized, and sintered in an electric furnace at 900 °C for 6 hours.

The phase structure of the ceramics was investigated by X-ray diffractometer (XRD; Panalytical Emperial, Malvern Panalytical Ltd., UK) using Cu-K_α (1.5406 Å) radiation in between 2θ=20-70 °C with scan speed 2 °C/min. The grain morphology of the ceramics was examined by scanning electron microscopy (FE-SEM; Gemini 500, Zeiss Corp., Germany). The elemental compositions were determined by scanning electron microscopy (SEM, JEOL, Tokyo, Japan, JSM-5910LV) equipped with energy dispersive spectroscopy (EDS, OXFORD Instruments, Abingdon, England, INCAx-Sight 7274; 133 eV resolution 5.9 keV) after Au (gold) coating. Frequency-dependent changes of real and imaginary permittivity and loss factor were investigated using dielectric equations:

$$\varepsilon' = \frac{C}{C_0}, \qquad \varepsilon'' = \frac{G}{\omega C_0}, \qquad C_0 = \varepsilon_0 \frac{A}{d} \quad \text{and} \quad tan\delta = \frac{\varepsilon''}{\varepsilon'}$$

where C_0 is vacuum capacitance, C is capacitance, w is angular frequency and G is conductance. The dielectric properties of the ceramic samples were carried out using an impedance analyzer (Wayne Kerr 6500 B Precision; between frequency 40 Hz–100 kHz, UK) at 1 Vrms potential at room temperature.

3. RESULTS AND DISCUSSION

3.1. XRD and SEM-EDS Results

Figure 1 presents the X-ray diffraction patterns of Eu^{3+}, and B^{3+} co-doped $CoNb_2O_6$ samples. XRD results of the ceramic samples were defined by orthorhombic columbite symmetry (JCPDS no: 32-0304) with space group *Pbcn*60. As seen in Figure 1, while 1 mol% concentration exhibits a single-phase $CoNb_2O_6$ structure, the $EuNbO_4$ secondary phase (JCPDS no: 22-1099) appears with increasing Eu^{3+} concentration. Additionally, the absence of boron-related reflections in the XRD results may be attributed to the dissolution of boron in the columbite structure, and similar studies have been reported (32,33). The schematic representation of the $CoNb_2O_6$ crystal structure consisting of corner-shared and edge-shared NbO_6 and CoO_6 octahedral is shown in Figure 2. In the columbite structure, there are three vacant octahedral sites labeled 4*a*, 4*b*, and 8*d*, where the 4*a* sites are the most favorable for Eu^{3+} occupancy (32-35). The XRD peaks of the (131) reflection are shown in Figure 3. With increasing Eu^{3+} concentration, a shift of the (131) peak to higher two theta angles was observed, which may be associated with a decrease in the lattice constant or the shrinkage of the lattice. The decrease in the lattice continued up to 9 mol%, while the shift to the left at 12 mol% indicated an expansion. Accordingly, the doping of Eu^{3+} ions will likely affect the charge balance due to the shrinkage of the lattice and cause some defects in the structure. Table 1 summarizes the lattice parameters of the samples, in which the *a*, *b*, *c*, and *V* data from 1 to 12 changed to 14.4995, 5.5857, 5.0559 Å, 409.47 $Å^3$ and 14.2362, 5.6138, 4.9888 Å, 398.70 $Å^3$, respectively. In addition, the cell data of orthorhombic $CoNb_2O_6$ are reported as a=14.167 Å, b=5.714 Å, c=5.046 Å, and V=408.47 $Å^3$ (27), which are consistent with the lattice parameters in this study. The average crystallite sizes of the samples from the Scherrer Eq. were found between 28.07 and 33.91 nm. The slight increase in crystallite size can be associated with the formation of a secondary $EuNbO_4$ phase due to the increased presence of Eu^{3+} and thus the development of crystallinity as a result of maintaining the charge balance in the structure.

Table 1: Cell parameters and crystallite sizes for Eu^{3+}, B^{3+} co-doped $CoNb_2O_6$ ceramics.

Sample (mol%)	Lattice parameters					Crystallite size
	a (Å)	*b* (Å)	*c* (Å)	*c*/a	*V* (Å)^3	*D* (nm)
Ref. [27]	14.1670	5.7140	5.0460	-	408.47	-
1 Eu^{3+}, 10 B^{3+}	14.4995	5.5857	5.0559	0.3487	409.47	28.07
3 Eu^{3+}, 10 B^{3+}	14.4058	5.5927	5.0492	0.3505	406.80	28.08
6 Eu^{3+}, 10 B^{3+}	14.2683	5.6033	5.0391	0.3532	402.87	29.79
9 Eu^{3+}, 10 B^{3+}	14.1471	5.6208	4.9822	0.3522	396.18	33.92
12 Eu^{3+}, 10 B^{3+}	14.2362	5.6138	4.9888	0.3504	398.70	33.91

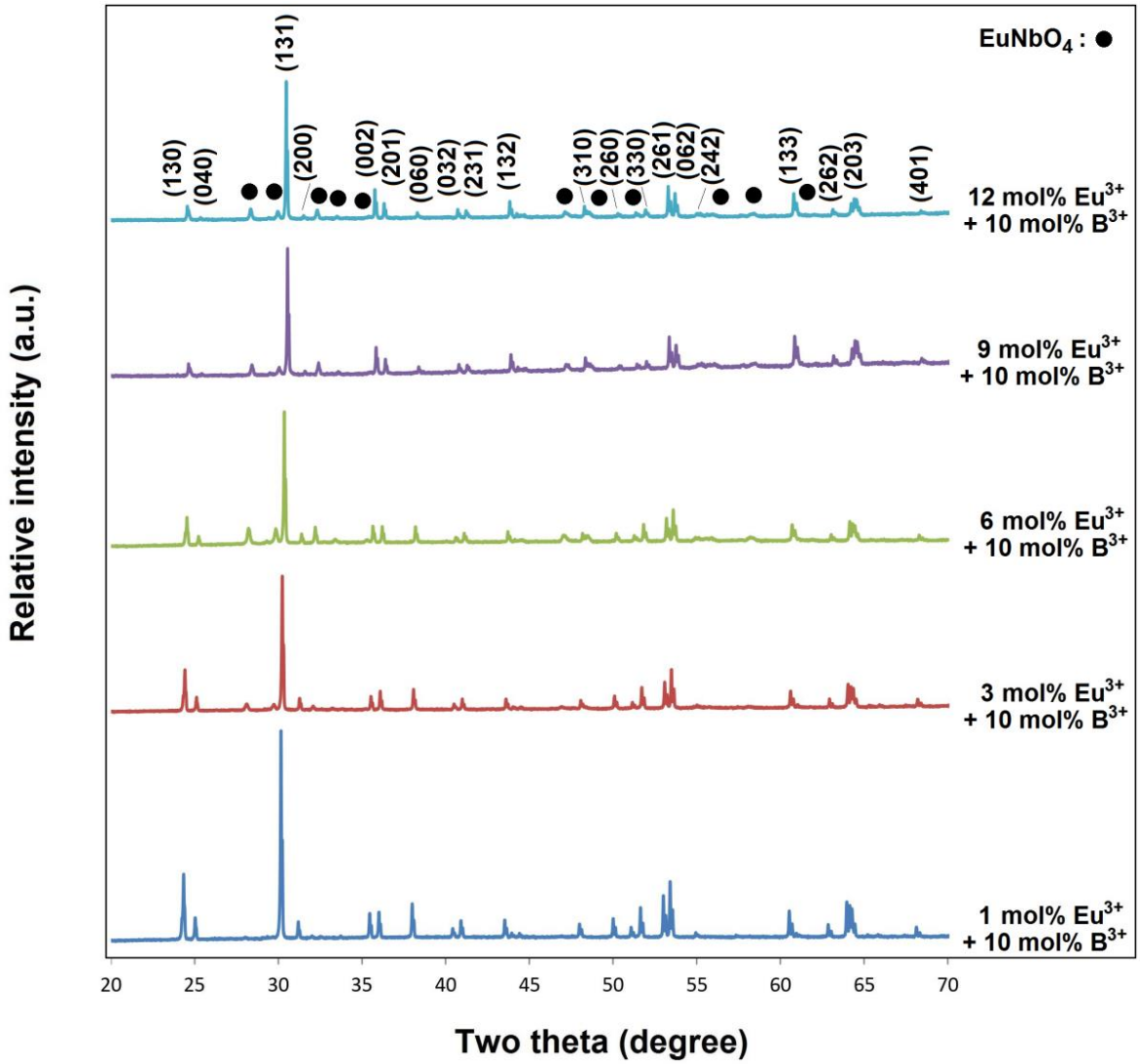

Figure 1: X-ray diffractions of $CoNb_2O_6$:*x*Eu^{3+},*y*B^{3+} (*x*=1, 3, 6, 9, 12 mol% Eu^{3+} , *y*=10 mol%) co-doped $CoNb_2O_6$ samples.

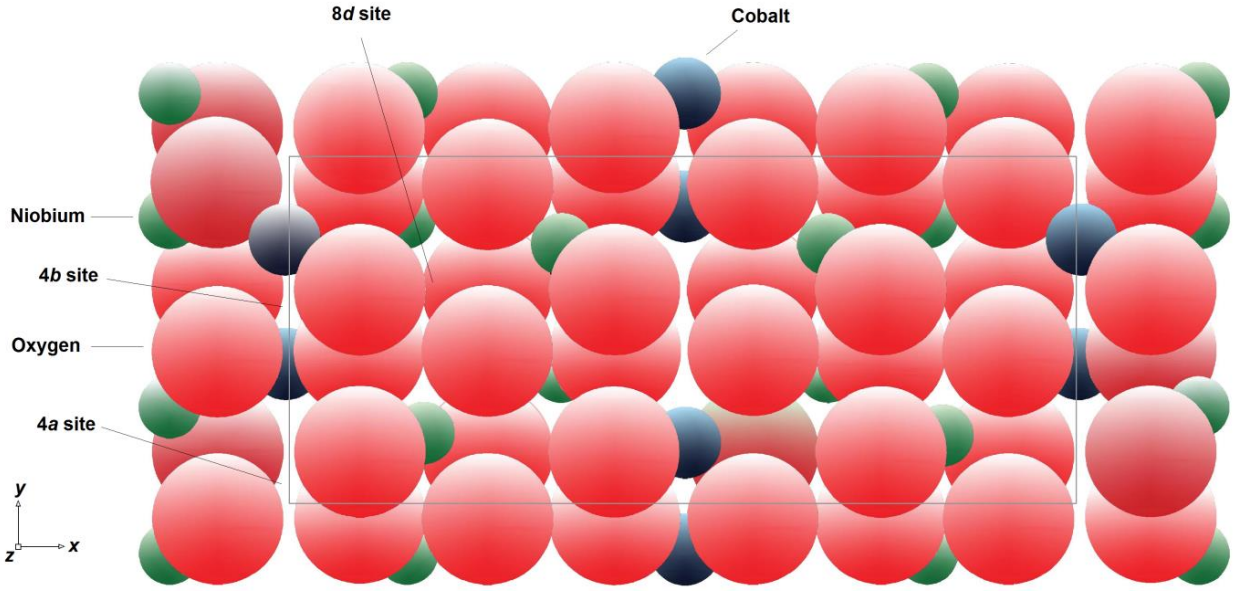

Figure 2: Schematic illustration of the $CoNb_2O_6$ crystal structure.

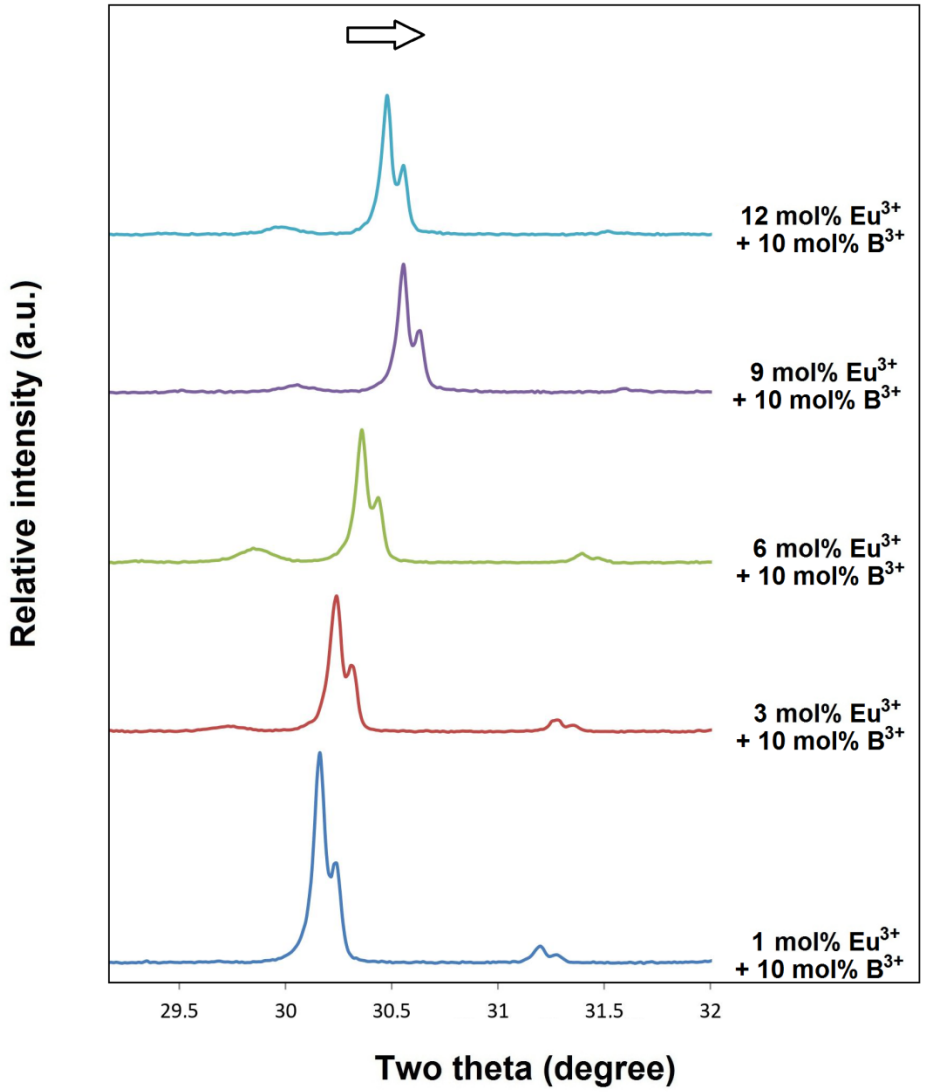

Figure 3: XRD two theta angles (131) shifted to higher angles with Eu^{3+} concentration.

Figure 4(a-e) shows the SEM micrographs at 5000x magnification for 1, 3, 6, 9 and 12 mol% Eu^{3+}, B^{3+} co-doped samples, respectively. In SEM micrographs, there was a slight increase in the grain sizes of the ceramic samples with the increasing Eu^{3+} concentration from 1 to 9 mol% which ranged between 1-30 μm. There was some decrease in grain sizes at 12 mol% concentration, while an increase

occurred in plate-shaped and elongated grains. Also, as seen in SEM micrographs in Figure 4(a-e), increasing Eu^{3+} concentration promotes the formation of collapses and holes in the grains. Moreover, it has been previously reported that the grain sizes of powder samples produced by the molten salt method at 800 °C are in the range of 0.05-2 μm (20). However, in this study, boron was subsequently added and the temperature was increased to 900 °C after pelletization. As a result, the morphology of the grains was affected by the 10 mol% boron doping, and increasing the temperature from 800 to 900 °C, a significant increase in grain sizes occurred.

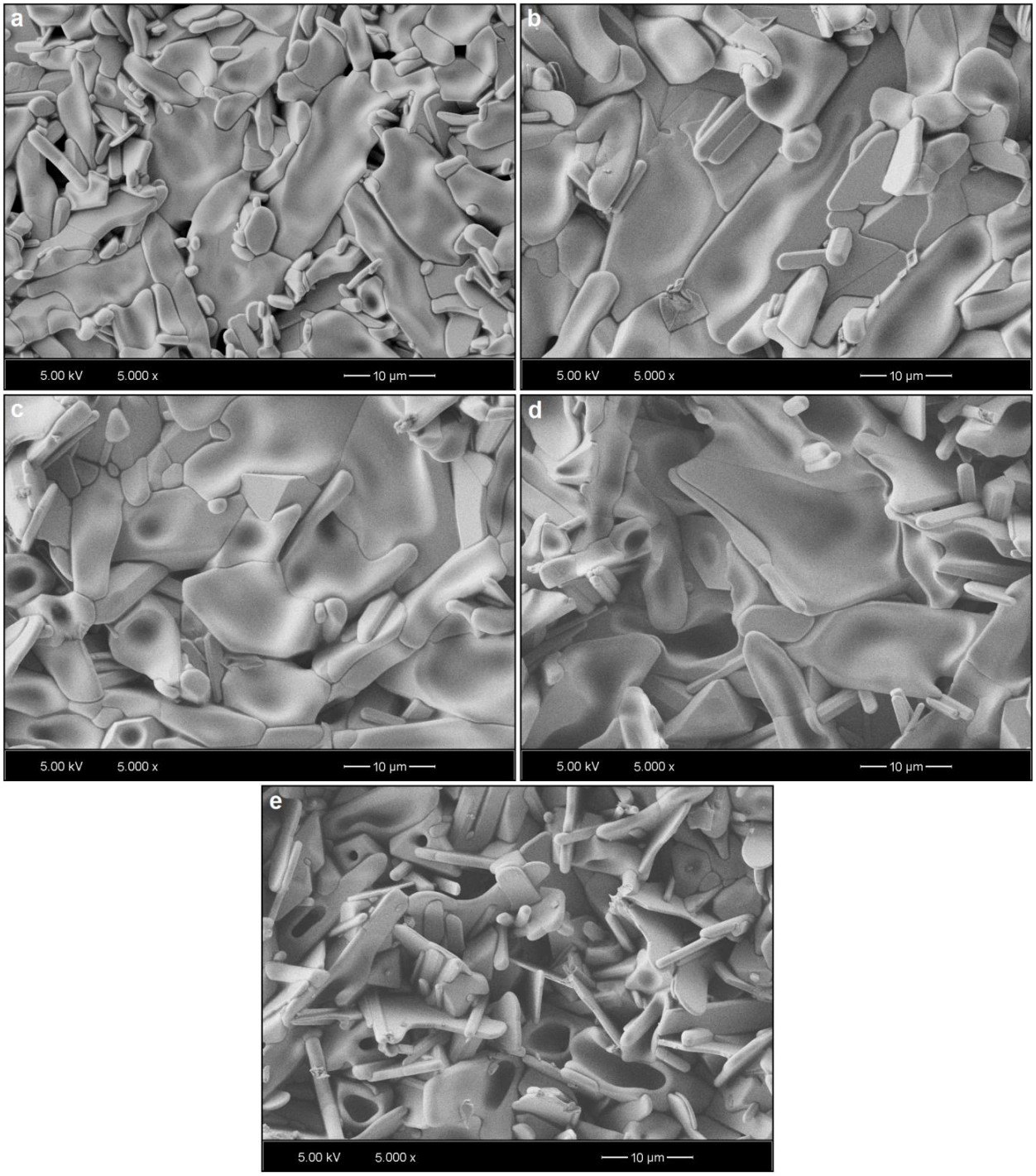

Figure 4: SEM micrographs of (a) 1, (b) 3, (c) 6, (d) 9, (e) 12 mol% Eu^{3+}, 10 mol% B^{3+} co-doped samples at 5000× magnifications and 5 kV acceleration voltage.

SEM-EDS analysis was performed to reveal phase structures and elemental compositions. Figure 5a shows an SEM micrograph for 6 mol% Eu^{3+}, 10 mol% B^{3+} co-doped sample, at 15000× magnification under 20 kV acceleration voltage. The elemental composition differences between $CoNb_2O_6$ main phase and $EuNbO_4$ minor phase were detected by EDS analysis, where the point-1 (Figure 5b) and point-2 (Figure 5c) show Eu^{3+} doped $CoNb_2O_6$ and $EuNbO_4$ grains, respectively. As seen from the EDS results, the atomic compositions (%) of the main and minor phases agree with the theoretical compositions (%).

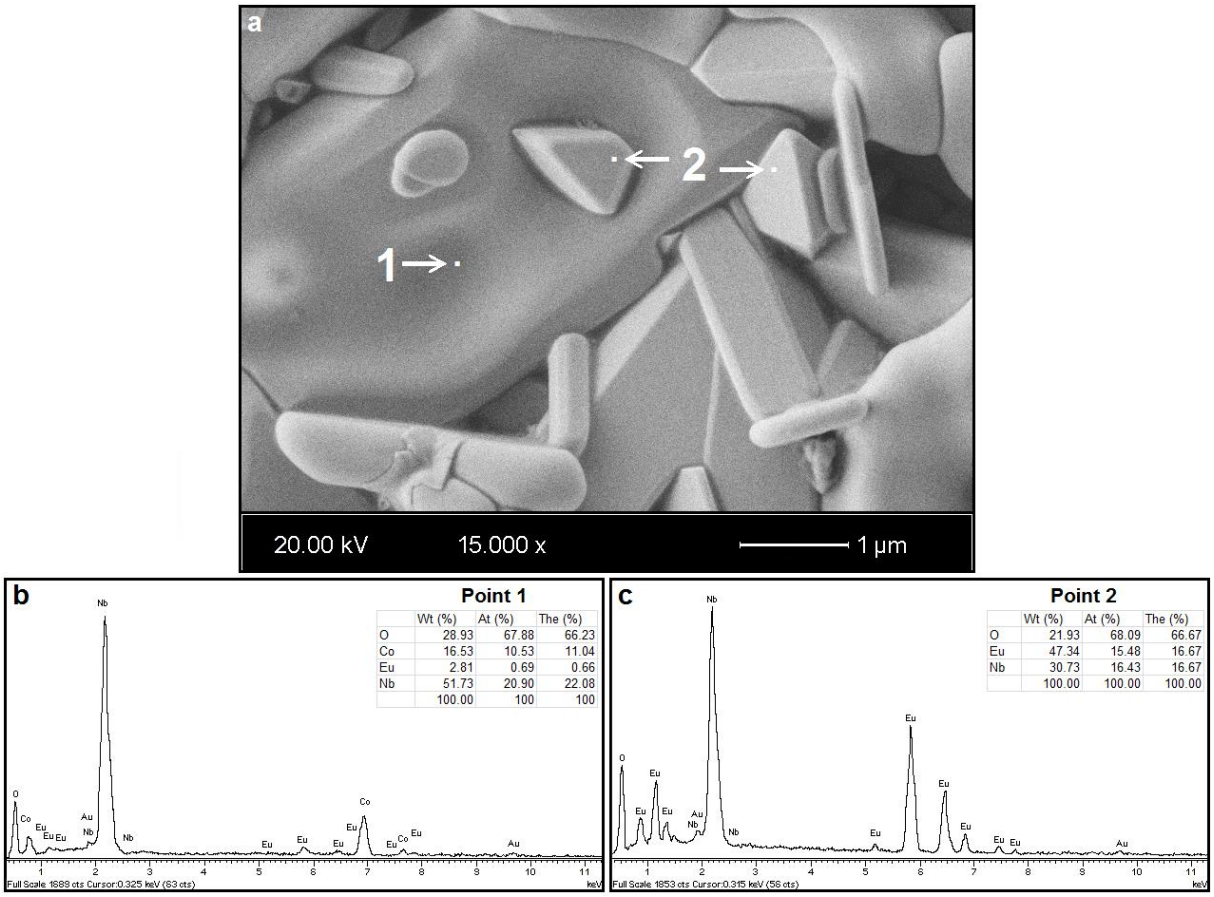

Figure 5: (a) SEM micrograph, and EDS spectrums with weight%, atomic% elemental compositions, and theoretical atomic% values, (b) main phase-point 1 (c) $EuNbO_4$ phase-point 2 for 6 mol% Eu^{3+}, 10 mol% B^{3+} co-doped sample.

3.2. Dielectric Behavior of Eu^{3+}, B^{3+} co-doped $CoNb_2O_6$ Ceramics

Figure 6 shows the dielectric constants (ε') of ceramic samples measured between 20 Hz–10^7 Hz. The dielectric constants of Eu^{3+}, and B^{3+} co-doped $CoNb_2O_6$ ceramics varied between approximately 34.8 and 24.5 at 20 Hz. As seen in Figure 6, the dielectric constant depends on frequency, the ε' value was almost constant in the high-frequency range, and it increased in the low-frequency range. Regarding this, with increasing frequency, the ability of electron exchange to follow the applied field, and therefore the dielectric constant decreases. At very high frequencies the field reverses before the motion of the space charge carriers and as a result, does not contribute to polarization, and so the ε' value is almost constant at high frequencies (36-38). In Figure 6, increasing Eu^{3+} concentration led to an increase in the dielectric constant up to 9 mol% and then decreased to 12 mol%. In a study conducted by Betinelli et al (39) on $BaTiO_3$, similar to this study, an increase in crystallite size and ε' value occurred with increasing Eu^{3+} concentration. So, Eu^{3+} ions are introduced into the host lattice as trivalent cations, giving rise to more point defects when increasing the dopant concentration, where the increasing ε' value with Eu^{3+} doping into the $BaTiO_3$ structure is attributed to the lattice defects caused by the dopant and is explained as the higher the lattice defects added to the host lattice with increasing dopant concentration, the higher the value of the dielectric constant. Accordingly, as seen in Figure 2 and Table 1, the shift to the right in the XRD peaks with increasing Eu^{3+} concentration can be associated with the presence of increasing defects in the lattice and the dielectric property improving up to 9 mol%. Moreover, the c/a ratio (40.41), which can be attributed to the distortion in the lattice, varies between 0.3487 and 0.3522 from 1 mol% to 9 mol%. On the other hand, as seen in Figure 2, the Eu^{3+} ions included in the structure caused a shift to the left or smaller two theta angles in the XRD peaks and expansion of the lattice, so a decrease occurred in the ε' value and c/a ratio at 12 mol% concentration. Based on this result, it is likely that a decrease in the dielectric constant occurred at 12 mol% Eu^{3+} concentration due to the presence of reduced point defects in the lattice. On the other hand, since the dielectric constant is grain size-related or sensitive to grain size and is affected externally, this phenomenon is explained based on the Maxwell-Wagner theory of extrinsic factors. According to this theory, the dielectric constant is directly proportional to the grain size of the sample, where an increase in grain size causes the polarization ability of atoms and the ε' value to increase (42-46). A slight increase in grain size in SEM examinations supports the improvement of the dielectric constant, which can be attributed to the absence of additional grain boundaries that prevent polarization. In addition, in the XRD results, it was previously stated that the formation of the $EuNbO_4$ secondary phase due to the increased presence of Eu^{3+} prevents the decrease in grain size by maintaining the charge balance in the

structure. This may be associated with a slight increase in the crystallite size, which supports the improved bulk feature and increased polarization. So, this increase in dielectric constant is considered to be consistent with the increase in grain size and crystallite size. As the amount of dopant increases, the grain size decreases, and the grain boundaries increase. At the same time, excessive grain boundary barrier weakens the electron transfer between grain boundaries and increases the interfacial polarization between grain and grain boundary, leading to deterioration of dielectric property (11). Of course, increasing dopant concentration will also increase the possibility of secondary phase formation, as in this study. The secondary phase effect is emphasized in detail in different studies in the literature (11,12). In a study on $(Nd_{0.5}Nb_{0.5})_xTi_{1-x}O_2$ by Wang et al (11), the secondary $NdTiNbO_6$ phase containing RE ions formed at x= 3% level and continued up to x= 7% concentration. Thus, the decrease in the dielectric constant after increasing up to x= 3% may be attributed to the tolerance of the secondary phase in the structure to some extent. In addition, the dielectric property of the secondary phase may affect the dielectric property of the main phase, like $RENbO_4$ ceramics which offer excellent dielectric properties (47). Therefore, the fact that the secondary phase of $EuNbO_4$ has dielectric properties, its increased presence in the structure or at grain boundaries may be ascribed to some extent being tolerated by the structure or reducing its deteriorating effect on the dielectric property.

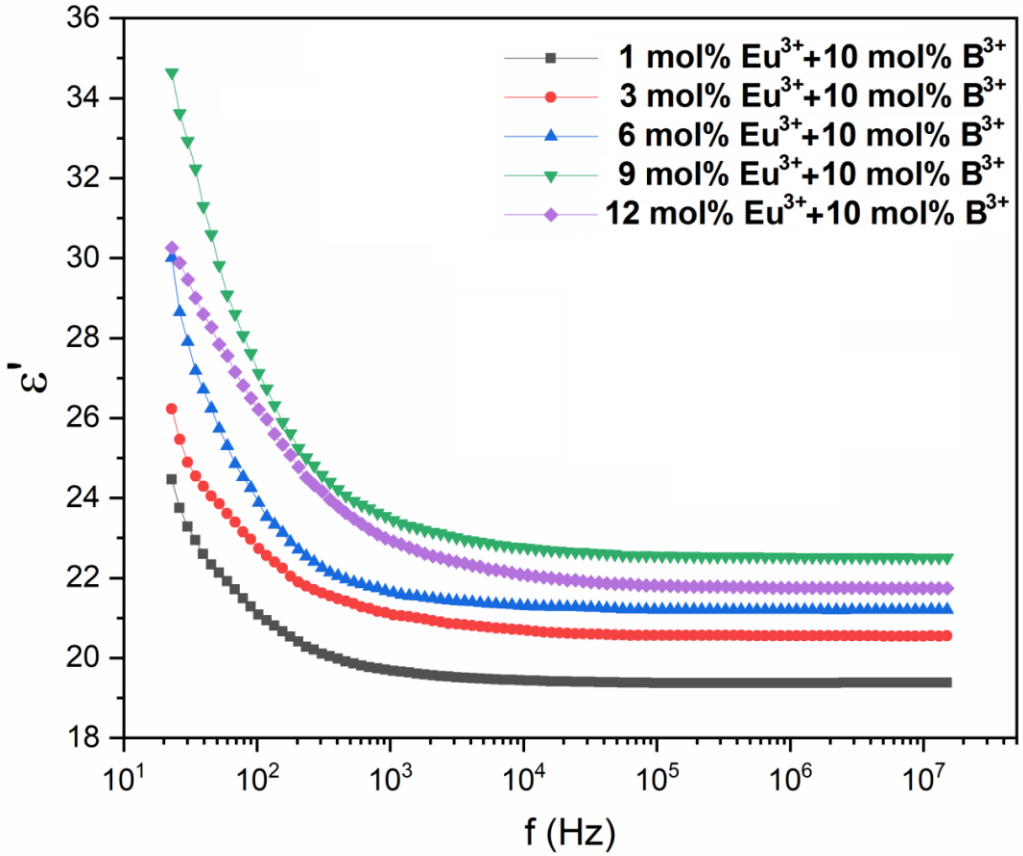

Figure 6: Dielectric constants of $CoNb_2O_6$:xEu^{3+}, yB^{3+} (x=1, 3, 6, 9, 12 mol%, y=10 mol% ceramics.

Figure 7 shows the variation of dielectric loss (tan δ) with frequency for Eu^{3+} doped $CoNb_2O_6$ samples. It is seen that dielectric loss increases continuously as the frequency decreases in the range of 20-10^5 Hz. In the low-frequency range corresponding to high resistance, more energy is required for polarization due to the grain boundary, while in the high-frequency range associated with low resistance, very little energy will be needed for electron transfer because of the grain boundary, and the energy loss will be less (48-50). The tan δ factor shows an increasing trend with increasing concentration up to 9 mol% Eu^{3+}. Different studies in the literature relate the dielectric loss factor in ferroelectrics to oxygen vacancies, which are responsible for dielectric loss or leakage current (50-53). The randomization or disorder of oxygen vacancies results in a decrease in the energy required for oxygen to jump from an occupied lattice site to an unoccupied site, so the oxygen vacancies in the structure undergo an order-disorder transition. This situation leads to an increase in ionic conductivity (53). Consequently, the increased dielectric loss may be related to Eu^{3+} substitution, which probably does not suppress oxygen vacancies or make them more ordered. This result led to an increase in ionic conductivity, and so increased dielectric loss or leakage current due to Eu^{3+} substitution. In addition, the decrease in dielectric loss at 12 mol% Eu^{3+} concentration may be associated with the Eu^{3+} substitution suppressing or making the oxygen vacancies more ordered.

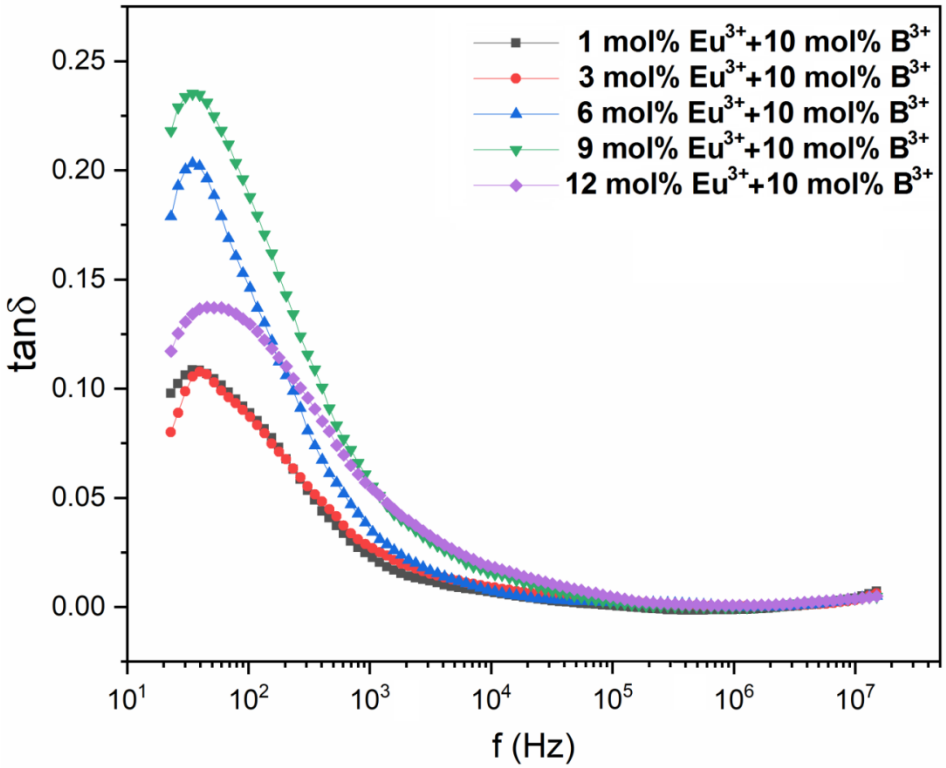

Figure 7: Dielectric losses of $CoNb_2O_6$:xEu^{3+}, yB^{3+} (x=1, 3, 6, 9, 12 mol%, y=10 mol% ceramics.

4. CONCLUSION

In the study, the structural and dielectric properties of orthorhombic columbite Eu^{3+}, and B^{3+} co-doped $CoNb_2O_6$ ceramics were examined. The powders were synthesized by the molten salt method at 800 °C, to improve the bulk property, boron was added and the sintering temperature was raised to 900 °C. In XRD results, the $CoNb_2O_6$ phase maintained up to 12 mol%, and also the $EuNbO_4$ minor phase was detected in which ceramic samples have slightly enhanced crystallinity. SEM micrographs showed that the Eu^{3+} increase led to a somewhat increase in grain sizes, while the formation of the plate-shaped and elongated morphology occurred in high Eu^{3+} concentrations. In EDS results, the atomic compositions (%) of the main and $EuNbO_4$ phases were agreed with the theoretical compositions (%). The dielectric constants of the Eu^{3+}, B^{3+} co-doped $CoNb_2O_6$ were determined in the range of 34.8 and 24.5 at 20 Hz, while increased Eu^{3+} caused an increase in the ε' value up to 9 mol% and then decreased for 12 mol%. Based on the evaluation of the Maxwell-Wagner theory, this increase in dielectric constant was considered to be consistent with the increase in grain size and crystallite size. The dielectric loss increased with increased Eu^{3+} concentration up to 9 mol%. The increased tan δ with increasing Eu^{3+} was attributed to Eu^{3+} substitution, which did not suppress oxygen vacancies or make them more ordered, and so this situation was associated with increased ionic conductivity and increased dielectric loss or leakage current.

5. CONFLICT OF INTEREST

There is no conflict of interest.

6. REFERENCES

1. Krohns S, Lunkenheimer P, Meissner S, Reller A, Gleich B, Rathgeber A, et al. The route to resource-efficient novel materials. Nat Mater [Internet]. 2011 Dec 23;10(12):899–901. Available from: <URL>.

2. Wersing W, Steele BCH. Electronic Ceramics. New York: Elsevier; 1991.

3. Hao S, Li J, Yang P, Wei L, Yang Z. Enhanced electrical properties and strong red light-emitting in Eu^{3+} -doped $Sr_{1.90}Ca_{0.15}Na_{0.9}Nb_5O_{15}$ ceramics. J Am Ceram Soc [Internet]. 2017 Dec;100(12):5620–8. Available from: <URL>.

4. İlhan M, Ekmekçi MK, Keskin İÇ. Judd–Ofelt parameters and X-ray irradiation results of MNb_2O_6:Eu^{3+} (M= Sr, Cd, Ni) phosphors synthesized *via* a molten salt method. RSC Adv [Internet]. 2021;11(18):10451–62. Available from: <URL>.

5. İlhan M, Katı Mİ, Keskin İÇ, Güleryüz LF. Evaluation of structural and spectroscopic results of tetragonal tungsten bronze MTa_2O_6:Eu^{3+} (M= Sr, Ba, Pb) phosphors and comparison on the basis of Judd-Ofelt parameters. J Alloys Compd [Internet]. 2022 Apr;901:163626. Available from: <URL>.

6. İlhan M, Keskin İÇ. Photoluminescence, radioluminescence and thermoluminescence properties of Eu^{3+} doped cadmium tantalate phosphor. Dalt Trans [Internet]. 2018;47(39):13939–48. Available from: <URL>.

7. Mahapatro J, Agrawal S. Effect of Eu^{3+} ions on electrical and dielectric properties of barium hexaferrites prepared by solution combustion method. Ceram Int [Internet]. 2021 Jul;47(14):20529–43. Available from: <URL>.

8. Evangeline T G, Annamalai A R, Ctibor P. Effect of Europium Addition on the Microstructure and Dielectric Properties of CCTO Ceramic Prepared Using Conventional and Microwave Sintering. Molecules [Internet]. 2023 Feb

8;28(4):1649. Available from: <URL>.

9. Chakrabarti A, Tarafder A, Molla AR. Synthesis of Eu^{3+} -doped $BaBi_2Ta_2O_9$ based glass-ceramic nanocomposites: Optical and dielectric properties. J Am Ceram Soc [Internet]. 2018 Jan 18;101(1):231–43. Available from: <URL>.

10. Fu J, Zhao J, Sa T, Qin N, Bao D. Photoluminescent and dielectric properties of Eu^{3+}-doped $LaAlO_3$ thin films fabricated by chemical solution deposition method. Appl Surf Sci [Internet]. 2013 Dec;286:1–6. Available from: <URL>.

11. Wang Z, Chen H, Nian W, Fan J, Li Y, Wang X, et al. Grain boundary effect on dielectric properties of $(Nd_{0.5}Nb_{0.5})_xTi_{1-x}O_2$ ceramicsceamics. J Alloys Compd [Internet]. 2019 May;785:875–82. Available from: <URL>.

12. Zhao C, Wu J. Effects of Secondary Phases on the High-Performance Colossal Permittivity in Titanium Dioxide Ceramics. ACS Appl Mater Interfaces [Internet]. 2018 Jan 31;10(4):3680–8. Available from: <URL>.

13. Sarvezuk PWC, Kinast EJ, Colin C V., Gusmão MA, da Cunha JBM, Isnard O. New investigation of the magnetic structure of $CoNb_2O_6$ columbite. J Appl Phys [Internet]. 2011 Apr 1;109(7):07E160. Available from: <URL>.

14. Scharf W, Weitzel H, Yaeger I, Maartense I, Wanklyn BM. Magnetic structures of $CoNb_2O_6$. J Magn Magn Mater [Internet]. 1979 Sep;13(1–2):121–4. Available from: <URL>.

15. Lei S, Wang C, Guo D, Gao X, Cheng D, Zhou J, et al. Synthesis and magnetic properties of MNb_2O_6 (M= Fe, Co, Ni) nanoparticles. RSC Adv [Internet]. 2014 Oct 13;4(95):52740–8. Available from: <URL>.

16. Xu Y, Wang LS, Huang YY, Ni JM, Zhao CC, Dai YF, et al. Quantum Critical Magnetic Excitations in Spin-1/2 and Spin-1 Chain Systems. Phys Rev X [Internet]. 2022 Apr 26;12(2):021020. Available from: <URL>.

17. Ringler JA, Kolesnikov AI, Ross KA. Single-ion properties of the transverse-field Ising model material $CoNb_2O_6$. Phys Rev B [Internet]. 2022 Jun 27;105(22):224421. Available from: <URL>.

18. Erdem R, İlhan M, Ekmekçi MK, Erdem Ö. Electrospinning, preparation and photoluminescence properties of $CoNb_2O_6$:Dy^{3+} incorporated polyamide 6 composite fibers. Appl Surf Sci [Internet]. 2017 Nov;421:240–6. Available from: <URL>.

19. Ekmekçi MK, İlhan M, Güleryüz LF, Mergen A. Study on molten salt synthesis, microstructural determination and white light emitting properties of $CoNb_2O_6$:Dy^{3+} phosphor. Optik (Stuttg) [Internet]. 2017 Jan;128:26–33. Available from: <URL>.

20. İlhan M, Güleryüz LF, Ekmekci MK. Structural Properties, Photoluminescence, and Judd-Ofelt Parameters of Eu^{3+}- Doped $CoNb_2O_6$ Phosphor. J Turkish Chem Soc Sect A Chem [Internet]. 2023 Aug 30;10(3):745–56. Available from: <URL>.

21. Ekmekçi MK, Erdem M, Başak AS. Molten salt synthesis, visible and near-IR region spectral properties of europium or neodymium doped $CoNb_2O_6$ columbite niobate. Dalt Trans [Internet]. 2015;44(12):5379–85. Available from: <URL>.

22. Singh N, Kumar K, Singh P. Synthesis of single phase Ti^{4+} substituted Trirutile $CoNb_2O_6$ Ceramic: evolution of Relaxor type ferroelectricity and high k dielectricity. J Electroceramics [Internet]. 2023 Oct 18;51(2):133–45. Available from: <URL>.

23. Zhang Y, Liu S, Zhang Y, Xiang M. Microwave dielectric properties of low-fired $CoNb_2O_6$ ceramics with B_2O_3 addition. J Mater Sci Mater Electron [Internet]. 2016 Nov 29;27(11):11293–8. Available from: <URL>.

24. Liu F, Wang B, Yang X, Guan Y, Sun R, Wang Q, et al. High-temperature stabilized zirconia-based sensors utilizing MNb_2O_6 (M: Co, Ni and Zn) sensing electrodes for detection of NO_2. Sensors Actuators B Chem [Internet]. 2016 Sep;232:523–30. Available from: <URL>.

25. Balamurugan C, Maheswari AR, Lee DW. Structural, optical, and selective ethanol sensing properties of p-type semiconducting CoNb2O6 nanopowder. Sensors Actuators B Chem [Internet]. 2014 Dec;205:289–97. Available from: <URL>.

26. Liang T, Koohpayeh SM, Krizan JW, McQueen TM, Cava RJ, Ong NP. Heat capacity peak at the quantum critical point of the transverse Ising magnet $CoNb_2O_6$. Nat Commun [Internet]. 2015 Jul 6;6(1):7611. Available from: <URL>.

27. Hanawa T, Shinkawa K, Ishikawa M, Miyatani K, Saito K, Kohn K. Anisotropic Specific Heat of $CoNb_2O_6$ in Magnetic Fields. J Phys Soc Japan [Internet]. 1994 Jul 15;63(7):2706–15. Available from: <URL>.

28. Zhang X, Wang B, Huang W, Chen Y, Wang G, Zeng L, et al. Synergistic Boron Doping of Semiconductor and Dielectric Layers for High-Performance Metal Oxide Transistors: Interplay of Experiment and Theory. J Am Chem Soc [Internet]. 2018 Oct 3;140(39):12501–10. Available from: <URL>.

29. Mazumder R, Seal A, Sen A, Maiti HS. Effect of Boron Addition on the Dielectric Properties of Giant Dielectric $CaCu_3Ti_4O_{12}$. Ferroelectrics [Internet]. 2005 Oct;326(1):103–8. Available from: <URL>.

30. Li Z, Zhou W, Su X, Luo F, Huang Y, Wang C. Effect of boron doping on microwave dielectric properties of SiC powder synthesized by combustion synthesis. J Alloys Compd [Internet]. 2011 Jan;509(3):973–6. Available from: <URL>.

31. İlhan M, Güleryüz LF. Boron doping effect on the structural, spectral properties and charge transfer mechanism of orthorhombic tungsten bronze β-$SrTa_2O_6$:Eu^{3+} phosphor. RSC Adv [Internet]. 2023;13(18):12375–85. Available from: <URL>.

32. İlhan M, Ekmekçi MK, Güleryüz LF. Effect of boron incorporation on the structural, morphological, and spectral properties of $CdNb_2O_6$:Dy^{3+} phosphor synthesized by molten salt process. Mater Sci Eng B [Internet]. 2023 Dec;298:116858. Available from: <URL>.

33. Başak AS, Ekmekçi MK, Erdem M, Ilhan M, Mergen A. Investigation of Boron-doping Effect on Photoluminescence Properties of $CdNb_2O_6$: Eu^{3+} Phosphors. J Fluoresc [Internet]. 2016 Mar 11;26(2):719–24. Available from: <URL>.

34. Ekmekçi MK, İlhan M, Ege A, Ayvacıklı M. Microstructural and Radioluminescence Characteristics of Nd^{3+} Doped Columbite-Type $SrNb_2O_6$ Phosphor. J Fluoresc [Internet]. 2017 May 13;27(3):973–9. Available from: <URL>.

35. İlhan M, Ekmekçi MK. Synthesis and photoluminescence properties of Dy^{3+} doped white light emitting $CdTa_2O_6$ phosphors. J Solid State Chem [Internet]. 2015 Mar;226:243–9. Available from: <URL>.

36. Tan YQ, Yu Y, Hao YM, Dong SY, Yang YW. Structure and dielectric properties of $Ba_5NdCu_{1.5}Nb_{8.5}O_{30}-\delta$ tungsten bronze ceramics. Mater Res Bull [Internet]. 2013 May;48(5):1934–8. Available from: <URL>.

37. Esha IN, Al-Amin M, Toma FTZ, Hossain E, Khan MNI, Maria KH. Synthesis and analysis of the influence of Eu^{3+} on the structural, ferromagnetic, dielectric and conductive characteristics of $Ni_{0.4}Zn_{0.45}Cu_{0.15}Fe_{(2-x)}Eu_xO_4$ composites using conventional double sintering ceramic method. J Ceram Process Res [Internet]. 2019 Oct;20(5):530–9. Available from: <URL>.

38. Shah MR, Akther Hossain AKM. Structural and dielectric properties of La substituted polycrystalline $Ca(Ti_{0.5}Fe_{0.5})O_3$. Mater Sci [Internet]. 2013 Jan 25;31(1):80–7. Available from: <URL>.

39. Bettinelli M, Speghini A, Seliman SI, Battisha IK. Structural and dielectrical properties of nano-structure BaTiO3 powders doped with Eu3+ ions prepared by sol-gel process. Fiz A a J Exp Theor Phys [Internet]. 2004 Mar 1;13(1):11–22. Available from: <URL>.

40. Kim L, Jung D, Kim J, Kim YS, Lee J. Strain manipulation in $BaTiO_3/SrTiO_3$ artificial lattice toward high dielectric constant and its nonlinearity. Appl Phys Lett [Internet]. 2003 Mar 31;82(13):2118–20. Available from: <URL>.

41. Feng L, Ye ZG. Phase Diagram and Phase Transitions in the Relaxor Ferroelectric $Pb(Fe_{2/3}W_{1/3})O_3–PbTiO_3$ System. J Solid State Chem [Internet]. 2002 Feb;163(2):484–90. Available from: <URL>.

42. Wagner KW. Zur Theorie der unvollkommenen Dielektrika. Ann Phys [Internet]. 1913 Jan 14;345(5):817–55. Available from: <URL>.

43. Maxwell JC. A treatise on electricity and magnetism. London: Caleredon press, Oxford University; 1873.

44. Kadam AA, Shinde SS, Yadav SP, Patil PS, Rajpure KY. Structural, morphological, electrical and magnetic properties of Dy doped Ni–Co substitutional spinel ferrite. J Magn Magn Mater [Internet]. 2013 Mar;329:59–64. Available from: <URL>.

45. Yuan WX, Luo Z, Wang C. Investigation on effects of CuO secondary phase on dielectric properties of $CaCu_3Ti_4O_{12}$ ceramics. J Alloys Compd [Internet]. 2013 Jun;562:1–4. Available from: <URL>.

46. Zheng Q, Fan H, Long C. Microstructures and electrical responses of pure and chromium-doped $CaCu_3Ti_4O_{12}$ ceramics. J Alloys Compd [Internet]. 2012 Jan;511(1):90–4. Available from: <URL>.

47. Liu L, Chen Y, Feng Z, Wu H, Zhang X. Crystal structure, infrared spectra, and microwave dielectric properties of the $EuNbO_4$ ceramic. Ceram Int [Internet]. 2021 Feb;47(3):4321–6. Available from: <URL>.

48. Gul IH, Maqsood A. Influence of Zn–Zr ions on physical and magnetic properties of co-precipitated cobalt ferrite nanoparticles. J Magn Magn Mater [Internet]. 2007 Sep;316(1):13–8. Available from: <URL>.

49. Ganguly P, Jha AK. Enhanced characteristics of $Ba_5SmTi_3Nb_7O_{30}$ ferroelectric nanocrystalline ceramic prepared by mechanical activation process: A comparative study. Mater Res Bull [Internet]. 2011 May;46(5):692–7. Available from: <URL>.

50. Sati PC, Kumar M, Chhoker S, Jewariya M. Influence of Eu substitution on structural, magnetic, optical and dielectric properties of $BiFeO_3$ multiferroic ceramics. Ceram Int [Internet]. 2015 Mar;41(2):2389–98. Available from: <URL>.

51. Chakrabarti A, Bera J. Effect of La-substitution on the structure and dielectric properties of $BaBi_4Ti_4O_{15}$ ceramics. J Alloys Compd [Internet]. 2010 Sep;505(2):668–74. Available from: <URL>.

52. Kumar P, Kar M. Effect of structural transition on magnetic and optical properties of Ca and Ti co-substituted $BiFeO_3$ ceramics. J Alloys Compd [Internet]. 2014 Jan;584:566–72. Available from: <URL>.

53. Kendall KR, Thomas JK, Loye HC. Synthesis and ionic conductivity of a new series of modified Aurivillius phases. Chem Mater [Internet]. 1995 Jan 1;7(1):50–7. Available from: <URL>.